JMEPEG (2012) 21:298–307
DOI: 10.1007/s11665-011-9929-9
©ASM International
1059-9495/$19.00

# Modeling Reaction Front Propagation and Porosity in Pressure-Assisted Combustion Synthesis of Porous NiTi Intermetallics

*Matthew Ballas, Zhiliang Li, and Olusegun J. Ilegbusi*

*(Submitted May 5, 2010; in revised form February 1, 2011)*

**A mathematical model is developed to investigate the effect of various processing parameters on pressure-assisted combustion synthesis of NiTi intermetallics. Specifically, preheat and ambient temperature, particle size, initial porosity, and pressure differential are studied to determine their influence on propagation behavior and final porosity. The governing equations are solved using a high-order-implicit numerical scheme capable of accommodating the steep spatial and temporal gradients of properties. The predicted results appear plausible and consistent with the trends presented in the available literature.**

**Keywords** combustion synthesis, particle growth, porous intermetallics, reaction kinetics, semi-solid slurry rheology

## 1. Introduction

During the latter half of the twentieth century, a variety of methods have been developed for the production of pure metal, alloy, and intermetallic foams (Ref 1-4). While these methods have performed well for many common alloys such as aluminum, they are typically far less successful when dealing with intermetallics due to the higher melting temperatures involved. Furthermore, most of these methods do not allow for the production of geometries any more complex than sheets or other simple profiles.

The process investigated hereinafter referred to as pressure-assisted combustion synthesis or PACS, addresses both of these concerns. The technique represents a novel variation of the conventional SHS in that it combines SHS and foaming in one operation to produce the porous material. This process, illustrated in Fig. 1, involves incorporating a high-pressure gas in the interstitial spaces of the unreacted elemental powders by backfilling the can prior to isostatic compaction. A similar approach has been applied to the foaming of superplastic Ti and Ti alloys but in the absence of chemical reaction or a liquid phase (Ref 1, 5). During combustion synthesis, the liquid phase will allow the high-pressure gas to expand the pores within an easily deformable semi-solid matrix, thus foaming the intermetallic compact. Here, the pore pressure is expected to increase the geometric uniformity of the pore structure as well as allow for precise control of the final porosity.

**Matthew Ballas, Zhiliang Li,** and **Olusegun J. Ilegbusi**, Department of Mechanical, Materials and Aerospace Engineering, University of Central Florida, Orlando, FL 32816-2450. Contact e-mail: ilegbusi@mail.ucf.edu.

The new idea involves incorporating a high pressure gas in the interstitial spaces of the unreacted elemental powders by backfilling the can prior to isostatic compaction. A similar approach has been applied to the foaming of superplastic Ti and Ti alloys but without chemical reaction or a liquid phase (Ref 1, 5). During combustion synthesis, the liquid phase will allow the high-pressure gas to expand the pores within an easily deformable semi-solid matrix, thus foaming the intermetallic compact.

There are two important benefits associated with the PACS process. First, pore growth in a semi-sold matrix is expected to significantly increase the geometric uniformity of the pore structure. Elzey and Wadley (Ref 6) have shown that the presence of a liquid phase during bubble growth in semi-solid alloys suppresses necking between adjacent bubbles in the material, thus reducing coalescence and irregularities at the pore surface. Secondly, the pressure-driven growth will allow for precise control of the final porosity (Ref 1, 5, 7). Proper control of the microstructure allows one to tailor the mechanical properties of the bulk material without adversely affecting its biocompatibility. Furthermore, this process will allow simultaneous chemical reaction and expansion of the product to the contours of a mold. Such capability is expected to be particularly useful in producing the complex geometries required for medical implants.

PACS involves a variety of mechanisms and subprocesses that have each been studied individually to some extent in the past. Among these, rheology in semi-solid slurries, general pore growth dynamics, and self-sustained high-temperature synthesis have copious representation in the literature. While under appropriate conditions the exothermic nature of the reaction allows the process to become steadily self-sustaining, SHS is very sensitive to the process parameters and material properties and other reaction patterns are possible (i.e., oscillatory propagation, fingering, and extinction) (Ref 7-10). In this study, the ratio of thermal conductivities on either side of the reaction front ($\kappa = k_p/k_r$) was found to directly affect the propagation behavior. For a moderately exothermic reaction such as Ni + Ti $\rightarrow$ NiTi, a conductivity ratio below a certain critical value results in an increasingly unstable propagation

front. Highly exothermic systems appear to be less affected by the conductivity ratio.

In this study, a numerical model is developed to simulate combustion synthesis with simultaneous pore growth driven by a pressure differential between the pore and the semi-solid alloy, $\Delta P$. The model is then used to elucidate the effect of important processing parameters on reaction propagation and pore morphology during PACS processing. Particular attention will be paid to preheat and ambient temperatures, particle size, pressure differential, and initial porosity.

## 2. Formulation

### 2.1 Physical Process

The PACS process is complex, involving a variety of physical phenomena across dimensional scales as illustrated in Fig. 2. These processes include macroscopic chemical reaction, pore growth in a semi-solid slurry intermediate phase, and heat transfer in a porous medium. A variety of approaches have been used to investigate the SHS process including microscopic mass transfer and material balances (Ref 11, 12). This study focuses on the chemical reaction front propagation and the pore growth characteristics, with the associated sub-processes. The physical phenomena in a generic combustion synthesis process have been presented in a previous article (Ref 13), as well as the routine used for numerical simulation. The study focused on the effect of reactant/product conductivity ratio on reaction front propagation and heat transfer in a one-dimensional cylindrical system. The present study provides a more comprehensive formulation of the PACS process in a one-dimensional cylindrical system. Specifically, the model formulation includes representation of phase transformation, rheology of the semi-slurry intermediate phase, as well as derivation of the equation for pore growth as a function of process parameters. There is allowance for heat loss by convection and radiation at the side surfaces.

The PACS model is built upon the basic algorithm developed for the combustion synthesis study discussed in Ref 13. As such, it utilizes the operator compact implicit

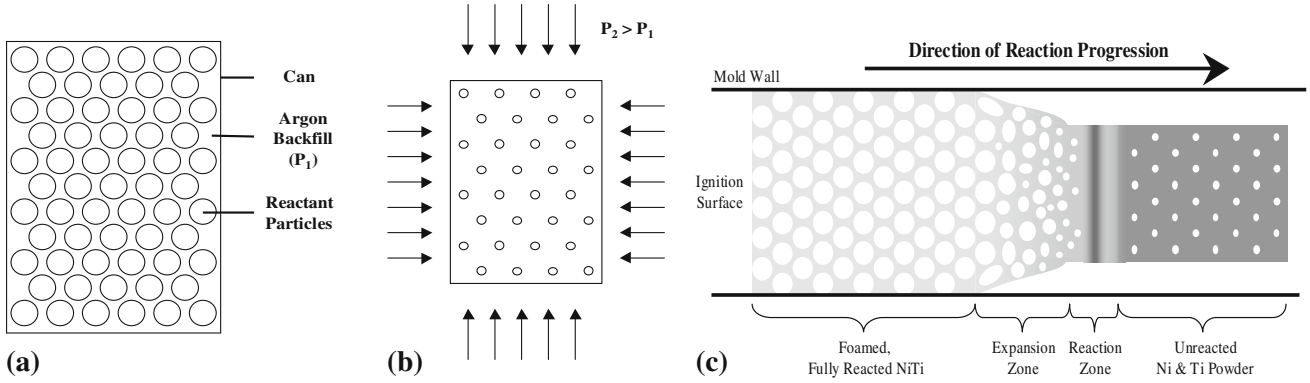


**Fig. 1** Schematic of the constrained pressure-assisted combustion synthesis (PACS) process. Ni and Ti particles are combined in an atmosphere of Ar (a), the can is then HIPed below the ignition point (b), and the resulting compact is ignited allowing the particles to react, forming porous NiTi (c)

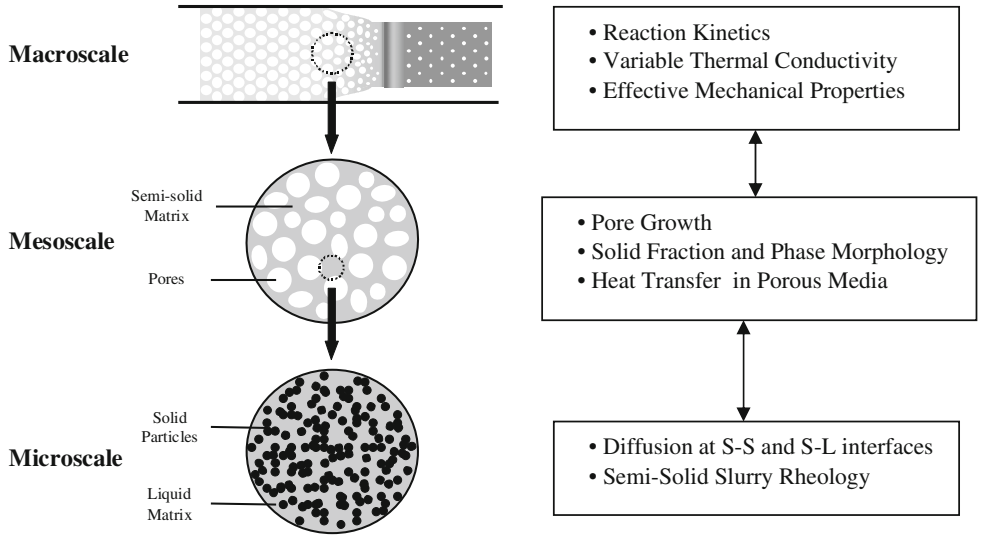


**Fig. 2** Schematic of multi-scale model for PACS process

method to resolve the steep temporal and spatial gradients. However, the current PACS model evaluates the energy equation in terms of enthalpy rather than temperature to more readily account for the various phases involved in the reaction. Furthermore, a number of additional subroutines are included to represent the constituent sub-processes. Important aspects of these subroutines utilized by the PACS model are described in the following sections.

### 2.2 Temperature-Enthalpy Phase Relationship for the NiTi System

Although the energy equation is evaluated in terms of enthalpy, temperature and solid fraction both play an important role in governing many of the subprocesses constituting PACS as illustrated in Fig. 2. For example, the total solid fraction has been shown to play an important role in determining the rate and extent of pore expansion (Ref 7, 14-16). Similarly, reactant ignition during combustion synthesis occurs at a specific temperature ($T_{ig}$ = 1183 K for NiTi) and the reaction rate itself is strongly temperature-dependent. Thus, the PACS model must be able to continually update the local temperature and solid fraction as the simulation progresses.

A linear interpolation scheme similar to that employed by Rao et al. (Ref 10) is used to calculate the temperature and solid fraction given the enthalpy and product fraction for a particular location in the system. In the interest of optimizing computation time, a constant specific heat is used for each of the phases involved in the reaction though temperature-dependent expressions can be easily incorporated at the expense of computational efficiency.

The interpolation scheme used in the PACS model begins by defining eight transition points as functions of the known local product fraction, $f_p$. Each transition point represents the limiting enthalpy corresponding to the onset or completion of a particular phase change:

- $h_1$ Ti is completely solid (α-phase). An increase in enthalpy leads to an allotropic phase change at constant temperature ($T_{1\text{-}2}$ = 1166 K, $Ti^{\alpha} \rightarrow Ti^{\beta}$)
- $h_2$ Ti is completely solid (β-phase). An increase in enthalpy leads to an increase in the temperature of the mixture ($\Delta T = (1/c_p)\Delta H$, 1166 K $\leq T \leq$ 1583 K)
- $h_3$ NiTi is completely solid. An increase in enthalpy leads to melting at constant temperature ($T_{3\text{-}4}$ = 1583 K, $NiTi^{s} \rightarrow NiTi^{l}$)
- $h_4$ NiTi is completely liquid. An increase in enthalpy leads to an increase in the temperature of the mixture ($\Delta T = (1/c_p)\Delta H$, 1583 K $\leq T \leq$ 1728 K)
- $h_5$ Ni is completely solid. An increase in enthalpy leads to melting at constant temperature ($T_{5\text{-}6}$ = 1728 K, $Ni^{s} \rightarrow Ni^{l}$)
- $h_6$ Ni is completely liquid. An increase in enthalpy leads to an increase in the temperature of the mixture ($\Delta T = (1/c_p)\Delta H$, 1728 K $\leq T \leq$ 1939 K)
- $h_7$ Ti is completely solid. An increase in enthalpy leads to melting at constant temperature ($T_{7\text{-}8}$ = 1939 K, $Ti^{\beta} \rightarrow Ti^{l}$)
- $h_8$ Ti is completely liquid. An increase in enthalpy leads to an increase in the temperature of the mixture

Once the transition enthalpies are known, the subroutine employed by the PACS model determines which region the known local enthalpy falls into. The nine regions can be subdivided into two groups. In the first group, the phase fractions remain constant and temperature is a linear function of enthalpy. In the second group, the temperature is known, and the phase fractions must be determined from the local enthalpy.

**2.2.1 Group 1: Variable Temperature.** When the enthalpy falls within a variable temperature range ($h < h_1$, $h_2 < h < h_3$, $h_4 < h < h_5$, $h_6 < h < h_7$, $h > h_8$), the phase fractions are fixed and the following expressions are used to calculate temperature:

$$c_p^{mix} = (1 - f_p)\left(c_p^{Ni} + c_p^{Ti}\right) + f_p\left(c_p^{NiTi}\right) \quad \text{(Eq 1)}$$

$$T_{mix} = T_n - \left(\frac{h_n - h}{c_p^{mix}}\right) \quad \text{(Eq 2)}$$

where $c_p^{mix}$ is the specific heat of the mixture, $T_{mix}$ is the temperature of the mixture, $T_n$ is the temperature corresponding to the reference transition enthalpy, $h_n$, and $h$ is the local enthalpy of the mixture. During this study, the upper bound transition enthalpy is used exclusively, thus $h_{n-1} < h < h_n$.

**2.2.2 Group 2: Phase Change.** When the enthalpy falls within a region of phase change ($h_3 < h < h_4$, $h_5 < h < h_6$, $h_7 < h < h_8$), the temperature is fixed accordingly and the following expression is used to calculate the appropriate phase fraction for constituent $X$:

$$f_{s,X} = f_X\left(\frac{h_X^L - h_X}{h_X^L - h_X^S}\right) \quad \text{(Eq 3)}$$

where $f_X$ is the is the volume fraction of constituent $X$. The superscripts L and S refer to the liquidus and solidus values, respectively.

### 2.3 Pore Growth

Due to the inherent nature of the NiTi system being investigated here, a fully solid, fully liquid, or semi-solid matrix may be present at any given time during the PACS process (Ref 17-20). The degree to which localized melting occurs depends strongly on the processing conditions. Thus, the pore growth subroutine developed for the PACS model considers three solid fraction regimes:

**2.3.1 Effectively Solid $f_s \geq 0.80$.** As a result of the moderate pressure differentials considered in this study, pore growth is assumed to be negligible at solid fractions above approximately 0.80. While pore expansion via high-temperature creep in the surrounding matrix is possible at such high solid fraction, the rate at which it occurs is insignificant considering the characteristic time of the process ($t_{ch} < 60$ s).

**2.3.2 Semi-Solid Slurry $0 \leq f_s \leq 0.80$.** Within this regime, two growth models apply given in Eq 4 and 5 (Ref 14, 21).

$$\dot{R} = \left\{\frac{P_b(R) - P_\infty - \frac{2\sigma}{R}}{4D(s_1)\frac{\left(f_s^{eff}(s_1)/f_s^{max}\right)^{1/3}}{1-\left(f_s^{eff}(s_1)/f_s^{max}\right)^{1/3}}\mu_l}\right\}R \quad \text{(Eq 4)}$$

$$\dot{R} = \left\{\frac{P_b(R) - P_\infty - \frac{2\sigma}{R}}{B\left[(1-m)(R^2/S^3)^{\frac{1}{m}} + m(1/R)^{\frac{1}{m}}\right]}\right\}^m \quad \text{(Eq 5)}$$

where

$$B = 4\left(2\sqrt{3}\right)^{\frac{m-1}{m}}\left(\frac{2}{\beta}\right)^{\frac{1}{m}}\alpha^{-1}A(f_s^*)^{-\frac{m+1}{2m}} * \exp\left(\frac{Q}{mR_GT}\right) \quad \text{(Eq 6)}$$

In the above equations, $\dot{R}$ is the growth rate of spherical bubble (pore), $R$ is pore radius, $P_b(R)$ is pressure inside the bubble, $P_\infty$ is the external pressure, σ is the surface tension at the gas-liquid interface, $s_1$ is the agglomeration parameter, $D(s_1)$ is the hydrodynamic coefficient (Ref 22), $f_s^{\text{eff}}(s_1)$ is the effective solid fraction, $f_s^{\max}$ is the maximum random packing fraction (~0.64), $\mu_l$ is the viscosity of the liquid phase, $m$ is the power law coefficient, $S$ is the cell radius (bubble plus a concentric liquid shell), α and β are material constants, $Q$ is the activation energy for vacancy formation and substitution diffusion in the alloy, and $R_G$ is the gas constant. Details of the derivation of these equations have been detailed in a companion paper (Ref 14).

In this study, the best approach is found to be one in which both models (Eq 4, 5) are used to generate reference growth rates ($\dot{R}_i^{\text{ref}}$) for a given set of local conditions including temperature and pressure differential. A representative $\dot{R} - f_s$ curve is interpolated from the reference values and the growth rate corresponding to the local solid fraction is then determined.

**2.3.3 Fully Liquid $f_s = 0$.** For the case of complete melting, the Newtonian pore growth model is used giving the following relation (Ref 14):

$$\dot{R} = \left\{\frac{P_b(R) - P_\infty - 2\sigma/R}{4a}\right\}R \quad \text{(Eq 7)}$$

where $a$ corresponds to the dynamic viscosity of the fluid.

During a simulation, the solid fraction is used to determine which growth model is applicable for a particular node. The local growth rate, $\dot{R}$, is then calculated and subsequently used to update the radius and porosity at the end of each time step.

### 2.4 Auxiliary Equations for Heat Transfer

Heat transfer through porous media is a complex problem involving simultaneous conduction, convection, and radiation. Previous combustion synthesis models have thus typically relied on a variety of methods to account for it. These methods range from using a single empirically determined effective thermal conductivity to far more complex representations involving percolation theory. One of the more rigorous approaches was developed by Zhang and Stangle (Ref 23) in which macroscopic (interporous) convection was included by representing the porous sample as a Bethe lattice and solving for the effective liquid-phase transport coefficient. Conduction and radiation were introduced separately and the corresponding coefficients were then summed to obtain the effective thermal conductivity in the sample. A simpler yet more common approach is to begin by making assumptions regarding the randomness or regularity of the pore microstructure. Zumbrunnen et al. (Ref 24) used this approach to simplify the problem by assuming that the porous structure resembled a regular array of evenly spaced/sized pores. This allowed for the derivation of a set of equations to account for both conduction through the solid phase and conduction/radiation across the pores (Ref 24, 25).

Due to the peculiarity of the NiTi system considered here in which only the product contributes to the liquid phase, interporous convection is not expected to play a significant role prior to reaction. Thus, the expressions based on those first derived by Zumbrunnen et al. (Ref 24) and later employed by Bhattacharya (Ref 25, 26) appear to be more appropriate for the present study.

Zumbrunnen et al.'s model is based on a statistical analysis of a regular array of pores. This model assumes a characteristic geometry in which the average pore size, $2R$, and the pore spacing (the average distance between the surfaces of two contiguous pores), $2\delta R$, are uniform throughout the system. However, the pore alignment in each successive row is allowed to vary. This gives rise to two distinct routes for heat flow through the system indicated by paths I and II. For a given distance across the array, path I intersects a pore in every row, whereas path II crosses only a single pore. Within this framework, the average number of pores contained in path I is given by:

$$\Gamma = 1 + \left(\ln\frac{\psi + 1}{\psi}\right)^{-1} \quad \text{(Eq 8)}$$

where ψ is the ratio of the average pore size to the pore spacing ($\psi = 2R/(2\delta R) = R/\delta R$). This ratio can be expressed in terms of the porosity, ϕ, as:

$$\psi = \frac{R}{\delta R} = \frac{\varphi^{1/3}}{1 - \varphi^{1/3}} \quad \text{(Eq 9)}$$

Likewise, the effective length for conduction through the matrix along path II is given by:

$$\Lambda = \frac{2R(1+\psi)\left[\frac{2+\psi}{1+\psi}\ln(1+\psi) + 1\right]}{\psi\ln(1+\psi)} \quad \text{(Eq 10)}$$

Using these expressions, Zumbrunnen et al. (Ref 24) defined a unit cell with an effective length of $\Gamma(1 + \psi) + \Lambda + 2R$. The unit cell was then modeled using a thermal resistance network in which the various resistances were weighted by the appropriate statistical factors (Eq 8, 10). The resultant expression for the effective local thermal conductivity in a porous medium is given by:

$$k_{\text{eff}} = \left[\lambda + \Gamma\left(\frac{\psi + 1}{\psi}\right) + 1\right] * \left[\frac{1}{k_m}\left(\frac{\Gamma\varsigma}{\psi} + \lambda\right) + (1 + \Gamma)\left(2Rh_r + \frac{k_f}{\xi}\right)^{-1}\right]^{-1} \quad \text{(Eq 11)}$$

where $k_m$ and $k_f$ are the thermal conductivities of the matrix material and pore fluid, respectively, ξ is an empirical parameter that relates conduction across the pores to the matrix conductivity, $h_r$ is the effective radiation heat transfer coefficient, and ζ is used to describe the pore morphology ($\zeta = 0$ for systems with open pores and $\zeta = 1$ for systems with closed pores). The parameter λ is the ratio of the effective matrix conduction length along path II to the average pore size:

$$\lambda = \frac{\Lambda}{2R} = \frac{(1+\psi)\left[\frac{2+\psi}{1+\psi}\ln(1+\psi) + 1\right]}{\psi\ln(1+\psi)} \quad \text{(Eq 12)}$$

### 2.5 Reaction Kinetics During Combustion Synthesis of NiTi

Self-propagating high-temperature synthesis relies on a reaction in which the local heat generation rate exceeds the local rate of heat redistribution, resulting in a temperature spike capable of igniting an adjacent layer of unreacted material and sustaining the process. During the reaction, the net local energy redistribution is the result of a combination of elementary processes. These processes include both endothermic reactions (melting of the reactants, $A$ and $B$ and/or product, $C$) and exothermic reactions (formation of the product, $C$, and mixing of $A$ and $B$ in $C$[1]). The balance between these elementary processes in combination with the local rate of heat transfer dictates both the reaction rate and the feasibility of sustaining the reaction through completion.

In modeling the PACS process, an $n$th order reaction rate equation similar to that proposed by Akiyama et al. is used (Ref 27):

$$\frac{\mathrm{d}f_\mathrm{p}}{\mathrm{d}t} = A\exp\left(-\frac{Q_\mathrm{r}}{R_\mathrm{G}T}\right)\left(1-f_\mathrm{p}\right)^n \qquad \text{(Eq 13)}$$

where $f_\mathrm{p}$ is the fraction of reacted material, $A$ is a pre-exponential factor, $Q_\mathrm{r}$ is the activation energy for the reaction, $R_\mathrm{G}$ is the gas constant, and $T$ is the local temperature. Although this expression fails to explicitly account for the individual processes involved in the reaction, it has been shown to provide very good agreement with the experimental data for a number of intermetallic systems (Ref 10, 28, 29).

For the specific case of NiTi, a second-order reaction was found to best fit the experimental data. It should be noted that during this study, simulations were performed using a first-order rate equation to elucidate the effect of $n$ on the final porosity. While reactions modeled with a first-order equation tend to propagate more quickly, differences between the final porosity for the two cases were found to be negligible.

### 2.6 Boundary Conditions

Prior to the evaluating the governing and auxiliary equations, boundary conditions must be specified at the exposed surfaces of the system. For the cylindrical geometry investigated in this study, there are three exposed surfaces to consider as illustrated in Fig. 3: the left and right faces and the circumferential boundary. These faces are referred to as *WEST*, *EAST*, and *NORTH*, respectively. The boundary and initial conditions used at these surfaces are given mathematically below, with $T_\infty$ being the ambient temperature and $T_0$ the initial temperature:

$$\text{WEST}: \quad T_{z=0,0<t\leq 2\mathrm{s}} = 2000K$$
$$T_{z=0,t>2\mathrm{s}} = T_\infty$$

$$\text{EAST}: T_{z=L,t\geq 0} = T_0$$

$$\text{Initial}: T_{z,t=0} = T_0$$

For the majority of simulations, synthesis is initiated by setting the temperature at the *WEST* boundary to a predetermined value well in excess of the ignition temperature ($T_\mathrm{W} > T_\mathrm{ig}$ = 1183 K). A value of $T_\mathrm{W}$ = 2000 K was found to provide a sufficient heating rate so as to ignite the reactants within approximately 1 to 2 s after simulation commencement. Following ignition, the *WEST* boundary temperature is brought down to the ambient temperature where it remains for the remainder of the simulation.

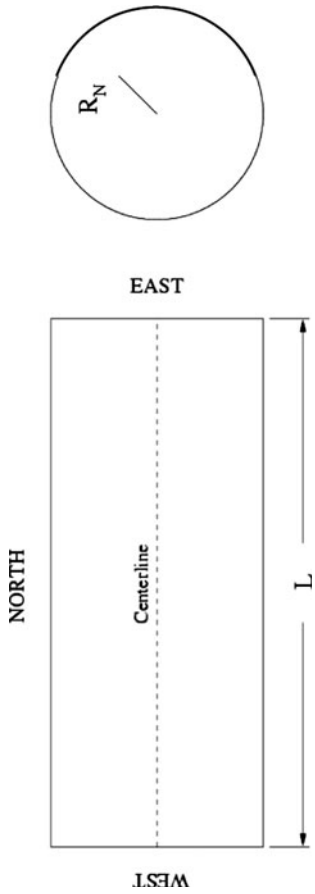


**Fig. 3** Schematic of the specimen geometry modeled in the PACS simulations

Typically, the temperature at the *EAST* boundary ($Z = L$) is set equal to the ambient/preheat temperature for the extent of the simulation. During simulations where the initial and ambient temperatures differ, the temperature at the *EAST* surface is set equal to the initial temperature, $T_0$.

Heat transfer at the *NORTH* boundary was incorporated in the PACS model as an additional source in the energy equation. The design of the algorithm allows the user to invoke convection, radiation, or both at the circumferential boundary. The source terms representing the convective and the radiative boundary conditions are defined as:

$$\dot{S}_\mathrm{conv} = -\frac{2h_\mathrm{eff}}{R_N}(T - T_\infty) \qquad \text{(Eq 14)}$$

and

$$\dot{S}_\mathrm{rad} = -\frac{2\sigma\varepsilon}{R_N}\left(T^4 - T_\infty^4\right) \qquad \text{(Eq 15)}$$

where $S$ is the additional source term, $h_\mathrm{eff}$ is the effective convection coefficient, $R_\mathrm{N}$ is the radius of the sample, $T$ is the surface temperature, $T_\infty$ is the ambient temperature, $\sigma$ is Stefan-Boltzmann constant, $\varepsilon$ is the emissivity at the surface, and the subscripts conv and rad refer to convection and radiation, respectively.

The PACS process investigated during this study involves reaction and pore expansion inside an argon-filled furnace held

at a constant temperature, $T\infty$. Thus, both convection and radiation were considered in the simulations. Assuming natural convection, an estimate of $h_{eff}$ = 10.0 W/m$^2$K is used in Eq 14 (Ref 30). Though the surface emissivity of unpolished NiTi was not found in the literature, a value of ε = 0.80 was considered to be reasonable (Ref 31).

### 2.7 Numerical Solution Procedure

The governing equations are solved numerically using a fully-implicit, finite difference formulation (Ref 13). This procedure requires integration of the differential equations over computational grids into which the sample has been discretized. The resulting algebraic equations are then solved using an algorithm based on the operator compact implicit formulation (Ref 32, 33). The algebraic equations are integrated over spatial and temporal grids that have been systematically optimized to obtain sufficient numerical accuracy of the solution. This process results in the choice of node spacings of $1.0 \times 10^{-6}$ m to $1.0 \times 10^{-5}$ m, corresponding to 1000 to 10,000 grid points, depending on the complexity of the specific reaction. The relevant thermophysical properties for the reactants and products are provided in Table 1.

## 3. Results and Discussions

Figure 4 to 6 shows output typical of the PACS model developed during this study. Figure 4 shows temperature profiles for the case of $L$ = 1 cm, $T_0$ = 1100 K, $T_\infty$ = 1100 K, initial porosity $\phi_0$ = 0.25, the Ni, Ti particle size $R_m$ = 144 μm, and the pore pressure to the ambient pressure ratio $P_0/P_\infty$ = 10, while Fig 5 and 6 presents the corresponding solid fraction and porosity profiles, respectively. Figure 4 depicts steady propagation profiles with maximum temperature $T_{max} = T_m^{NiTi}$ = 1583 K and velocity $v_{ss}$ = 0.844 cm/s. The steady reaction front results in the smooth solid fraction and porosity profiles shown in the subsequent figures. Figure 5 indicates a minimum solid fraction of $f_s$ = 0.350 except near the EAST and WEST boundaries which were kept at constant temperature. In Fig. 6, the corresponding final porosity is seen to reach a maximum value of $\phi_f$ = 0.547 before matrix solidification prevents further pore growth.

It should be noted that steady propagation profiles similar to those shown in Fig. 4 to 6 were observed for all cases investigated during this study regardless of initial temperature, porosity, or pressure differential. However, the latent heat of melting limits energy redistribution and thus restricts heat transfer ahead of the reaction front. The excessive heat transfer ahead of the reaction front was linked with premature bulk ignition and oscillatory propagation (Ref 13). By concentrating most of the available energy in the reaction region rather than allowing it to conduct ahead of the front, partial melting helps to offset the effect of initial porosity during PACS processing.

Figure 7 to 9 depicts the preheat temperature and particle size dependence of three process variables: reaction front propagation velocity, minimum solid fraction, and final porosity. Figure 7 shows the reaction front propagation velocity ($v_{ss}$) as a function of preheat temperature ($T_0$) for $R_m$ = 1.0, 10.0, 50.0, and 100.0 μm. While propagation velocity is seen to increase slightly with increasing preheat temperature for all four cases, the particle radius appears to have a much greater effect on propagation velocity. This behavior is particularly evident for $R_m > 10.0$ μm and is likely the result of increased heat transfer due to radiation across the pores. The larger pores tend to increase the effective thermal conductivity in a porous medium at high temperature. Experimental evidence obtained in standard combustion synthesis studies suggests that a higher

**Table 1 Material properties used in the PACS computations**

| Component | ρ, kg/m$^3$ | $c_p$, kJ/kg K | $k$, W/mK | Reference |
|---|---|---|---|---|
| Ni | 8900 | 443.60 (S)<br>662.94 (L) | 90.4 | (Ref 31, 32) |
| Ti | 4500 | 530.80 (α-S)<br>780.70 (β-S)<br>986.63 (L) | 22.3 | (Ref 31, 32) |
| NiTi | 6450 | 629.45 (S)<br>705.52 (L) | 10.0 | (Ref 32) |
| Ar (pores) | 1.784 | | 0.01772 | (Ref 31) |

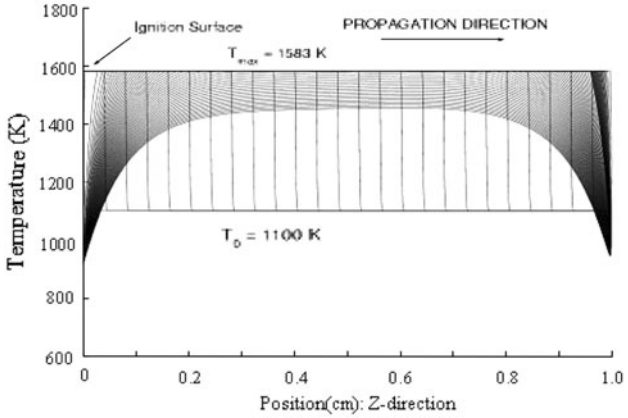


**Fig. 4** Temperature profiles generated by the PACS model for the case of $T_0$ = 1100 K, $T_\infty$ = 1100 K, $\phi_0$ = 0.25, $R_m$ = 144 μm, and $P_0/P_\infty$ = 10. Reaction phase: $\Delta t_r = 4.8 \times 10^{-2}$s. Expansion/cooling phase: $\Delta t_e = 2.0 \times 10^{-1}$ s

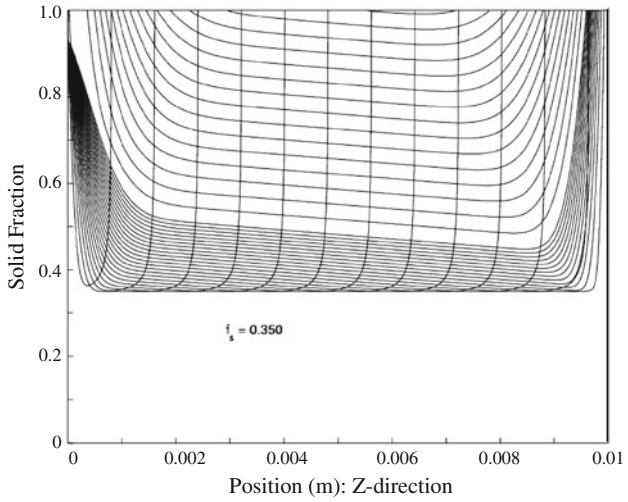


**Fig. 5** Solid fraction profiles generated by the PACS model for the case of $T_0$ = 1100 K, $T_\infty$ = 1100 K, $\phi_0$ = 0.25, $R_m$ = 144 μm, and $P_0/P_\infty$ = 10. Reaction phase: $\Delta t_r = 4.8 \times 10^{-2}$ s. Expansion/cooling phase: $\Delta t_e = 2.0 \times 10^{-1}$ s

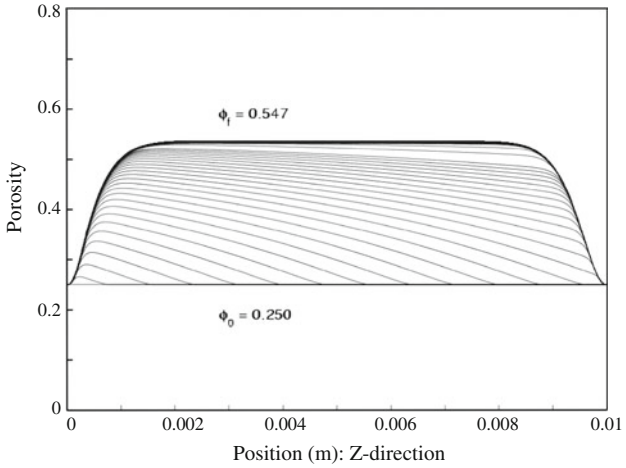


**Fig. 6** Porosity profiles generated by the PACS model for the case of $T_0$ = 1100 K, $T_\infty$ = 1100 K, $\phi_0$ = 0.25, $R_m$ = 144 μm, and $P_0/P_\infty$ = 10. Reaction phase: $\Delta t_r = 4.8 \times 10^{-2}$ s. Expansion/cooling phase: $\Delta t_e = 2.0 \times 10^{-1}$ s

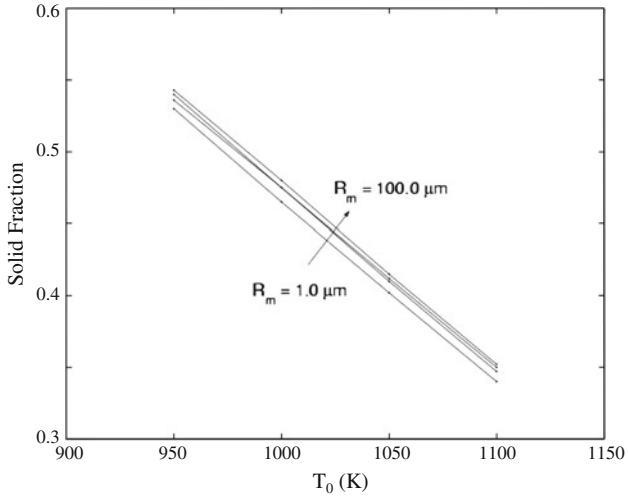


**Fig. 8** Minimum solid fraction versus initial temperature for the case of $\phi_0$ = 0.25, $T_\infty = T_0$, and $P_0/P_\infty$ = 10 showing the effect of particle size

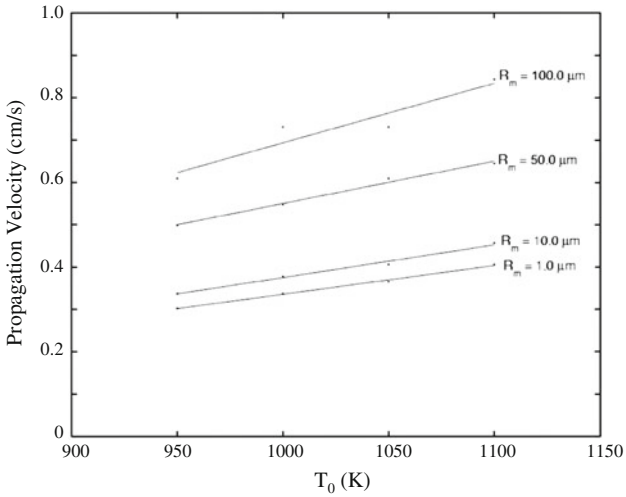


**Fig. 7** Propagation velocity versus initial temperature for the case of $\phi_0$ = 0.25, $T_\infty = T_0$, and $P_0/P_\infty$ = 10 showing the effect of particle size

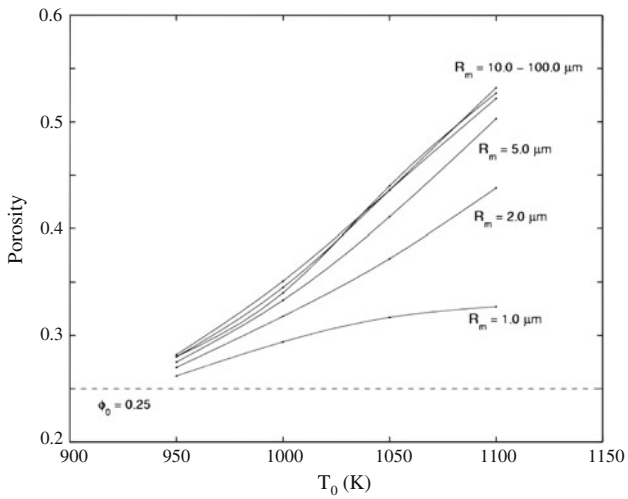


**Fig. 9** Final porosity versus initial temperature for the case of $\phi_0$ = 0.25, $T_\infty = T_0$, and $P_0/P_\infty$ = 10 showing the effect of particle size

thermal conductivity leads to faster propagation velocities, thus supporting the results shown here.

Figure 8 shows the effect of preheat temperature and particle size on the minimum solid fraction, $f_s^{min}$. As would be expected, an increase in preheat temperature results in a decrease in solid fraction. Less anticipated is the fact that particle size appears to have some effect on the solid fraction. Specifically, a smaller average particle size results in a slightly lower solid fraction. This implies that a finer powder helps to concentrate heat in the reaction front. A courser powder, with a larger corresponding pore size, results in a larger effective conductivity ahead of the reaction front and thus more heat is allowed to leak from the reaction zone. All other factors being equal, this suggests that using a smaller particle size for the powder compact will result in a higher final porosity.

Figure 9 shows final porosity, $\phi_f$, as a function of preheat temperature and particle size. Above $R_m$ = 10.0 μm, there is a nearly linear correlation between porosity and initial temperature. Increasing preheat temperature results in a lower solid fraction and a higher final porosity. Within this regime, particle size does not appear to have a significant effect on porosity. However, porosity does exhibit a strong particle size dependence for $R_m < 10.0$ μm. This is particularly evident at higher preheat temperatures. For the case of $R_m$ = 1.0 μm and $T_0$ = 1100 K, porosity rises from $\phi_0$ = 0.250 to $\phi_f$ = 0.330, an increase of only a 32% (compared to a nearly 115% increase for $R_m \geq 10.0$ μm). These observations suggest the importance of surface tension at the gas-matrix interface. For a constant initial porosity, a smaller average particle radius corresponds to a smaller initial pore size. For small enough pore radii, the surface tension term in the pore growth equations (Ref 14) is in the same order as the pressure differential. The effective driving force for pore expansion is thus significantly reduced, thereby inhibiting pore growth. For most practical applications, powder sizes in the range $25 < R_m < 100.0$ μm are typically the norm,

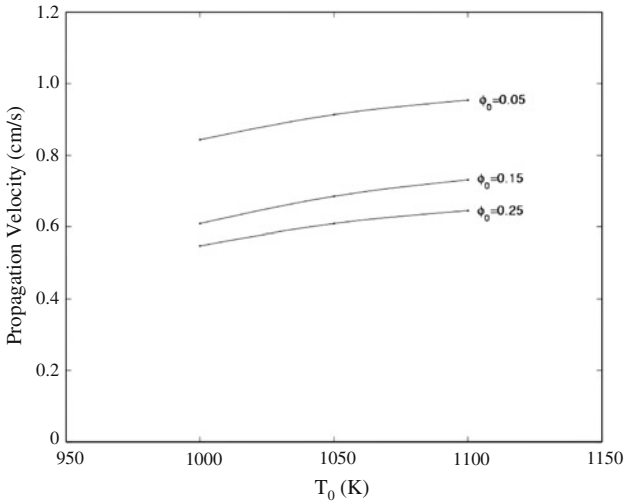


**Fig. 10** Effect of $P_0$ and $\phi_0$ on the temperature dependence of propagation velocity for $R_m$ = 50 μm and $P_\infty$ = 1 atm

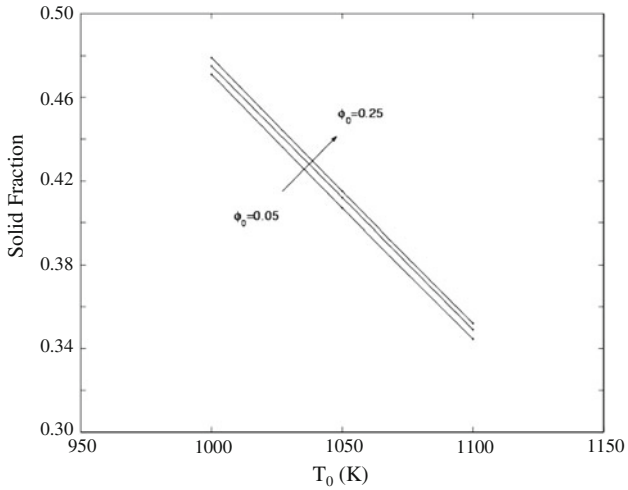


**Fig. 11** Effect of $P_0$ and $\phi_0$ on the temperature dependence of solid fraction for $R_m$ = 50 μm and $P_\infty$ = 1 atm

corresponding to initial pore radii in the range $17.3 < R_0 < 69.3$ μm at $\phi = 0.25$. Thus, the effect of surface tension is not normally expected to be an important factor. However, if circumstances dictate the use of smaller particle sizes, the effect of surface tension must be considered.

Figure 10 to 12 illustrates the effect of initial pore pressure, $P_0$, and porosity, $\phi_0$, on the temperature dependence of the propagation velocity, solid fraction, and final porosity. In Fig. 10, the increase in propagation velocity with initial temperature seen earlier is again evident at all three initial porosities ($\phi_0$ = 0.05, 0.15, and 0.25). In addition, Fig. 10 shows a significant increase in propagation velocity with lower initial porosity. Regardless of the initial temperature, the propagation velocity nearly doubles with a porosity decrease from $\phi_0$ = 0.25 to 0.05. It should be noted that the propagation curves for $P_0$ = 5, 10, and 30 atm are identical for the same initial porosity. Thus, the initial pore pressure appears to have no effect on the propagation velocity.

Figure 11 shows the effect of preheat temperature, initial pressure, and initial porosity on the minimum solid fraction. As was the case in Fig. 10, curves for the different initial pore pressures are identical for the same initial porosity. However, the initial porosity does have an effect on the solid fraction with a lower initial porosity resulting in a lower minimum solid fraction. This can be explained by the effective thermal conductivity model. A higher initial porosity allows more heat to escape from the reaction zone via radiation across the pores. Thus, the extent of melting in the reaction front is somewhat less than would be the case for a lower initial porosity. As a result, it is reasonable to expect that pores will be more likely to expand to the maximum allowable radius in the case of lower initial porosity.

Figure 12 shows final porosity as a function of preheat temperature for $P_0$ = 5, 10, and 30 atm and initial $\phi_0$ = 0.05, 0.15, and 0.25. Clearly, a higher initial pressure leads to a larger porosity increase in all the cases considered. Also anticipated is the fact that a higher initial porosity results in a higher final porosity assuming the same initial pore pressure ($\phi_f$ ($\phi_0$ = 0.05) < $\phi_f$ ($\phi_0$ = 0.15) < $\phi_f$ ($\phi_0$ = 0.25) for $P_0(\phi_0 = 0.05) = P_0(\phi_0 = 0.15) = P_0(\phi_0 = 0.25)$). However, it is interesting to note that the preheat temperature dependence of final porosity is more

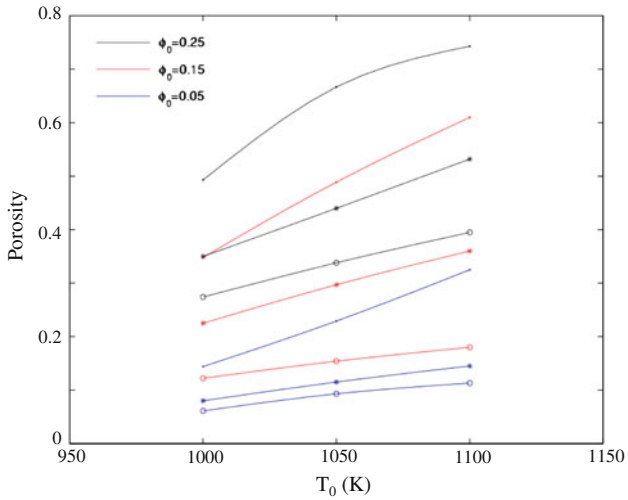


**Fig. 12** Effect of $P_0$ and $\phi_0$ on the temperature dependence of porosity for $R_m$ = 50 μm and $P_\infty$ = 1 atm: $P_0$ = 30 atm (·), $P_0$ = 10 atm (*), and $P_0$ = 5 atm (○)

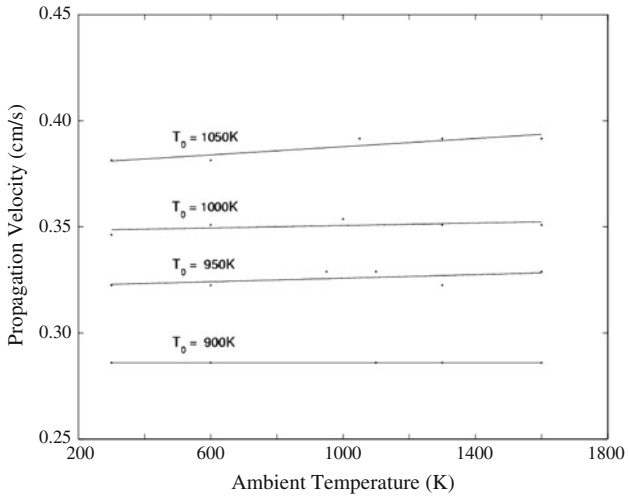


**Fig. 13** Effect of $T_\infty$ on the temperature dependence of propagation velocity for $R_m$ = 1 μm and $P_0$ = 10 atm

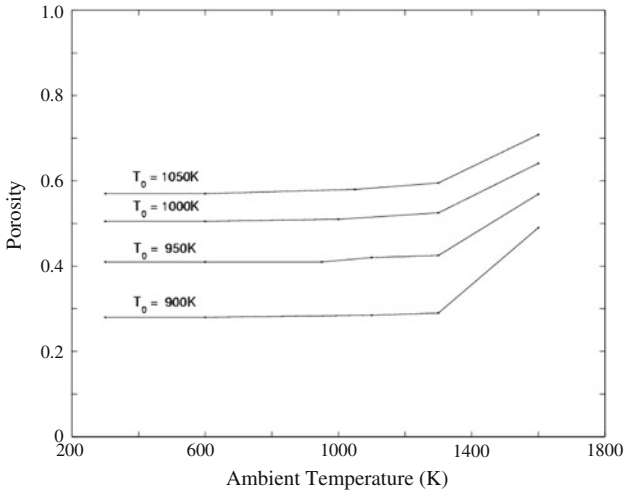


**Fig. 14** Effect of $T_\infty$ on the temperature dependence of porosity for $R_m$ = 1 μm and $P_0$ = 10 atm

prominent at higher initial porosity. This is likely due to the increased effect of radiation at higher initial porosity. The lower propagation velocity associated with a higher initial porosity means that a particular region within the sample will spend more time in the semi-solid state. Thus, pores are allowed more time to undergo expansion.

Finally, Fig. 13 and 14 shows the effect of ambient temperature ($T_\infty$) on the PACS process. Figure 13 suggests that the ambient temperature does not significantly influence the propagation velocity. This is expected because for the ambient temperature to have any effect, the sample would have to lose enough heat to the surroundings so as to reduce the initial temperature at a given location before the reaction front arrives. Due to the relatively fast propagation velocity, the sample does not have enough time to cool off significantly prior to the completion of the reaction.

Figure 14 illustrates the effect of ambient temperature on the final porosity. For $T_\infty < T_m^{NiTi}$ (=1583 K), final porosity does not appear to be a function of $T_\infty$. However, porosity tends to increase in cases where the ambient temperature is above the melting point of the product. This is the result of post-reaction heating in which the high ambient temperature continues to melt the specimen long after the completion of the reaction. The extended time during which the product remains partially liquid allows the pores to continue expanding.

## 4. Conclusions

The effect of various processing parameters on PACS of NiTi has been investigated. Specifically, preheat and ambient temperature, particle size, initial porosity, and pressure differential were studied to determine their influence on propagation behavior and final porosity. A numerical model was developed to simulate the process, taking into account variations in porosity as the reaction progresses. The governing equations were solved using a high-order-implicit numerical scheme capable of accommodating the steep spatial and temporal gradients of properties. The predicted results appear plausible and consistent with the trends presented in the available literature. However, a direct comparison with the experimental data was impossible due to the novelty of the process.

The major findings of the study may be summarized thus:

- An increase in the preheat temperature results in a higher front propagation velocity, lower minimum solid fraction, and higher final porosity.
- Increasing the particle size leads to a higher front propagation velocity, higher minimum solid fraction, and higher final porosity
- The effect of surface tension at the gas matrix interface becomes increasingly evident with decreasing particle size (corresponding to a decreasing pore size).
- A lower initial porosity results in a higher front propagation velocity, lower minimum solid fraction, and lower final porosity.
- Preheat temperature has a greater effect on final porosity with increasing initial porosity.
- Initial pore pressure, $P_0$, has no effect on the propagation velocity, $v_{ss}$, or minimum solid fraction, $f_s^{min}$.
- Ambient temperature has no discernable effect on propagation behavior.

The results obtained in this study help to further characterize the behavior of self-sustaining high-temperature synthesis in general as well as provide guidance in specifying stable and acceptable processing paths for the combustion synthesis of porous intermetallics. Preheat temperature, particle size, initial porosity, and pore pressure, have all been shown to significantly affect propagation behavior and final porosity during PACS processing. Thus, it should be feasible to use these variables to control the porous microstructure, thereby dictating the mechanical properties of the final product.

## References

1. D.C. Dunand and J. Teisen, Superplastic Foaming of Titanium and Ti-6Al-4V, *Porous and Cellular Materials for Structural Applications*, D.S. Schwartz, D.S. Shih, A.G. Evans, and H.N.G. Wadley, Ed., Materials Research Society, Warrendale, PA, 1998, p 231–236
2. J. Barnhart and J. Baumeister, Production Methods for Metallic Foams, *Porous and Cellular Materials for Structural Applications*, D.S. Schwartz, D.S. Shih, A.G. Evans, and H.N.G. Wadley, Ed., Materials Research Society, Warrendale, PA, 1998, p 121–132
3. G.J. Davies and S. Zhen, Metal Foams: Their Production, Properties and Applications, *J. Mater. Sci.*, 1983, **18**(7), p 1899–1911
4. V.I. Shapavalov, Formation of Ordered Gas-Solid Structures Via Solidification in Metal-Hydrogen Systems, *Porous and Cellular Materials for Structural Applications*, D.S. Schwartz, D.S. Shih, A.G. Evans, and H.N.G. Wadley, Ed., Materials Research Society, Warrendale, PA, 1998, p 281–290
5. N.G. Davis, J. Teisen, C. Schuh, and D.C. Dunand, Solid State Foaming of Titanium by Superplastic Expansion of Argon-Filled Pores, *J. Mater. Res.*, 2001, **16**(5), p 1508–1519
6. D.M. Elzey and H.N.G. Wadley, The Limits of Solid State Foaming, *Acta Mater.*, 2001, **49**(5), p 849–859
7. C.L. Yeh and C.C. Yeh, Preparation of CoAl Intermetallic Compound by Combustion Synthesis in Self-Propagating Mode, *J. Alloys Compd.*, 2005, **288**, p 241–249
8. J. Puszynski, J. Degreve, and V. Hlavacek, Modeling of Exothermic Solid-Solid Noncatalytic Reactions, *Ind. Eng. Chem. Res.*, 1987, **26**(7), p 1424–1434
9. J. Puszynski, V.K. Jayaraman, and V. Hlavacek, A Stefan Problem for Exothermic Non-Catalytic Reactions, *Int. J. Heat Mass Transf.*, 1985, **28**(6), p 1237–1239

10. L. Rao, P. Yu, and R.B. Kaner, Numerical Modeling of Combustion Synthesis with Phase Changes, *J. Mater. Synth. Process.*, 1994, **2**(6), p 343–353
11. A.M. Locci, A. Cincotti, F. Delogu, and R. Orru, Combustion Synthesis of Metal Carbides: Part I, Model Development, *J. Mater. Res.*, 2005, **20**(5), p 1257–1268
12. A.M. Locci, A. Cincotti, F. Delogu, and R. Orru, Combustion Synthesis of Metal Carbides: Part II, Numerical Simulation and Comparison with Experimental Data, *J. Mater. Res.*, 2005, **20**(5), p 1269–1277
13. M. Ballas, H. Song, and O.J. Ilegbusi, Effect of Thermal Conductivity on Reaction Front Propagation During Combustion Synthesis of Intermetallic, *J. Mater. Sci.*, 2006, **41**(13), p 4169–4177
14. O.J. Ilegbusi and M.W. Ballas, Modeling Pore Growth in Semi-Solid Alloy Foams, *J. Mater. Process. Technol.*, 2006, **178**, p 88–97
15. C. Zanotti, P. Giuliani, A. Terrosu, S. Gennari, and F. Maglia, Porous Ni-Ti Ignition and Combustion Synthesis, *Intermetallics*, 2007, **15**, p 404–412
16. N. Bertolino, M. Monagheddu, A. Tacca, P. Giuliani, C. Zanotti, and U.A. Tamburini, Ignition Mechanism in Combustion Synthesis of Ti-Al and Ti-Ni Systems, *Intermetallics*, 2003, **11**, p 41
17. J.C. van der Werff and C.G. de Kruif, Hard Sphere Colloidal Dispersions: The Scaling of Rheological Properties with Particle Size, Volume Fraction, and Shear Rate, *J. Rheol.*, 1989, **33**(3), p 421–454
18. H.C. Yi and J.J. Moore, The Combustion Synthesis of Ni–Ti Shape Memory Alloys, *J. Miner. Met. Mater. Soc.*, 1990, **42**(8), p 31–35
19. H.C. Yi and J.J. Moore, Combustion Synthesis of TiNi Intermetallic Compounds Part 1: Determination of Heat of Fusion of TiNi and Heat Capacity of Liquid TiNi, *J. Mater. Sci.*, 1989, **24**(10), p 3449–3455
20. H.C. Yi and J.J. Moore, A Novel Technique for Producing NiTi Shape Memory Alloy using the Thermal Explosion Mode of Combustion Synthesis, *Scripta Metall.*, 1988, **22**(12), p 1889–1892
21. O.J. Ilegbusi and M.W. Ballas, A Hybrid Constitutive Model for Semi-Solid Alloy Slurries, *J. Mater. Process. Manuf. Sci.*, 2000, **8**(1), p 18–33
22. P. Kumar, C.L. Martin, and S. Brown, Constitutive Modeling and Characterization of the Flow Behavior of Semi-Solid Metal Alloy Slurries-I. The Flow Response, *Acta Metall. Mater.*, 1994, **42**(11), p 3595–3602
23. Y. Zhang and G.C. Stangle, A Micromechanistic Model of the Combustion Synthesis Process: Part I. Theoretical Development, *J. Mater. Res.*, 1994, **9**(10), p 2592–2604
24. D.A. Zumbrunnen, R. Viskanta, and F.P. Incropera, Heat Transfer Through Porous Solids with Complex Internal Geometries, *Int. J. Heat Mass Transf.*, 1986, **29**(2), p 275–284
25. A.K. Bhattacharya, Green Density of a Powder Compact and Its Influence on the Steady-State Wave Velocity in Combustion Synthesis of Condensed Phase, *J. Am. Ceram. Soc.*, 1991, **74**(9), p 2113–2116
26. A.K. Bhattacharya, Modelling of the Effects of Porosity and Particle Size on the Steady-State Wave Velocity in Combustion Synthesis, *J. Mater. Sci.*, 1992, **27**(6), p 1521–1527
27. T. Akiyama, H. Isogai, and J. Yagi, Reaction Rate of Combustion Synthesis of an Intermetallic Compound, *Powder Metall.*, 1998, **95**(2), p 175–181
28. T. Akiyama, H. Isogai, and J. Yagi, Mathematical Model of Combustion Synthesis, *AIChE J.*, 1998, **44**(3), p 695–700
29. Z.A. Munir, Reaction Synthesis Processes: Mechanisms and Characteristics, *Metall. Trans.*, 1992, **23A**(1), p 7–13
30. F.P. Incropera and D.P. De Witt, *Introduction to Heat Transfer*, 2nd ed., Wiley, New York, 1990
31. R. Siegel and J.R. Howell, *Thermal Radiation Heat Transfer*, 3rd ed., Hemisphere Publication Corp, Washington, DC, 1992
32. M. Ciment, S.H. Leventhal, and B.C. Weinberg, The Operator Compact Implicit Method for Parabolic Equations, *J. Comput. Phys.*, 1978, **28**(2), p 135–166
33. R.S. Hirsh, Higher Order Accurate Difference Solutions of Fluid Mechanics Problems by a Compact Differencing Technique, *J. Comput. Phys.*, 1975, **19**(1), p 90–109